

NUMERICAL SIMULATIONS OF DRIVEN RELATIVISTIC MHD TURBULENCE

JONATHAN ZRAKE AND ANDREW I. MACFADYEN

Center for Cosmology and Particle Physics, Physics Department, New York University, New York, NY 10003, USA
Draft version October 28, 2018

ABSTRACT

A wide variety of astrophysical phenomena involve the flow of turbulent magnetized gas with relativistic velocity or energy density. Examples include gamma-ray bursts, active galactic nuclei, pulsars, magnetars, micro-quasars, merging neutron stars, X-ray binaries, some supernovae, and the early universe. In order to elucidate the basic properties of the relativistic magnetohydrodynamical (RMHD) turbulence present in these systems, we present results from numerical simulations of fully developed driven turbulence in a relativistically warm, weakly magnetized and mildly compressible ideal fluid. We have evolved the RMHD equations for many dynamical times on a uniform grid with 1024^3 zones using a high order Godunov code. We observe the growth of magnetic energy from a seed field through saturation at $\sim 1\%$ of the total fluid energy. We compute the power spectrum of velocity and density-weighted velocity $U = \rho^{1/3}v$ and conclude that the inertial scaling is consistent with a slope of $-5/3$. We compute the longitudinal and transverse velocity structure functions of order p up to 11, and discuss their possible deviation from the expected scaling for non-relativistic media. We also compute the scale-dependent distortion of coherent velocity structures with respect to the local magnetic field, finding a weaker scale dependence than is expected for incompressible non-relativistic flows with a strong mean field.

Subject headings: hydrodynamics — magnetohydrodynamics — methods: numerical — gamma-ray burst: general — turbulence

1. INTRODUCTION

Turbulence is a fundamental open problem in classical physics and is of broad importance in science and technology. While non-relativistic turbulence has been studied in great detail (e.g., Davidson 2004), relatively little attention has been devoted to the properties of turbulence in relativistic gas. Yet gas flows in astrophysics are known to be relativistic and turbulent in a wide variety of systems under active investigation. Extensive evidence of relativistic gas flow now exists, most dramatically in astronomical observations of outflows from gamma-ray bursts (GRBs) (see recent reviews by Piran 2004; Fox & Mészáros 2006; Woosley & Bloom 2006; Zhang & Mészáros 2004; Gehrels et al. 2009) and active galactic nuclei (e.g. Begelman et al. 1984; Antonucci 1993; Krolik 1999; Frank et al. 2002). Nearer by, relativistic outflows are observed from a variety of sources including micro-quasars, soft gamma repeaters (SGRs), and some supernovae (Soderberg et al. 2010). Theoretical models for the central engines powering a broad range of astrophysical phenomena invoke gas accretion onto black holes and neutron stars. In addition, the gravitational wave sources targeted by LIGO involve the hydrodynamical merging of neutron star–neutron star or neutron star–black hole binaries. The merging of neutron star binaries generates shear as the stars touch and merge. Shear is also generated as neutron stars are shredded when merging with a black hole binary companion. Kelvin-Helmholtz instability in these shear flows generate turbulence which can lead to large amplifications of magnetic field (Zhang et al. 2009). Such field amplification may be crucial for creating conditions capable of extracting observed luminosities from the GRB central engine (Gehrels et al. 2009).

Many astrophysical flows, including the aforementioned, are at least partially relativistic (bulk and/or thermal Lorentz factor $\gtrsim 1$) and all are highly susceptible to turbulence due to the extremely high Reynolds numbers characterizing astrophysical gas. Knowledge of the properties of relativistic turbulence is also of general importance in physics, with direct applications to early universe cosmology, heavy ion colliders, and high energy density physics and laboratory plasmas. Research elucidating the basic properties of relativistic turbulence is thus broadly motivated.

In order to advance knowledge of turbulence in the largely unexplored relativistic case, we have begun a series of numerical simulations of turbulent flows in magnetized gas with relativistic energy density or velocity. In this first in a series of papers on this topic we present simulations and analysis of driven turbulence in a transonic, super-Alfvénic medium for which the ratio of internal to rest mass energy density is of order unity. Differences from non-relativistic turbulence may be expected since pressure and magnetic fluctuations communicated by acoustic and MHD waves modify the fluid inertial term in the relativistic case. This is distinct from the non-relativistic case where fluid inertia is proportional to rest mass density but does not depend on internal energy, pressure or magnetic field strength.

We have studied the same model (SATS1) at a range of resolutions up to 1024^3 in order to demonstrate numerical convergence. We make comparisons with the extensive body of literature available for compressible non-relativistic hydrodynamic and MHD turbulence (e.g., Padoan et al. 1997; Vazquez-Semadeni et al. 2000; Cho & Lazarian 2003; Beresnyak et al. 2005; Kritsuk et al. 2007, 2009; Schmidt et al. 2008;

Federrath et al. 2010; Lemaster & Stone 2009; Burkhart et al. 2009; Kowal & Lazarian 2010). We also draw from studies of Alfvénic turbulence in the non-relativistic (e.g., Politano et al. 1995; Cho & Vishniac 2000a; Maron & Goldreich 2001; Beresnyak et al. 2005; Beresnyak & Lazarian 2009, 2010) and relativistic force-free (Cho 2005) regimes. By applying the same analyses utilized in these studies to our own models, our aim is to elucidate the similarities and differences existing between the relativistic and non-relativistic limit of MHD turbulence.

This paper is organized as follows: In §2 we provide the details of our computational scheme and problem setup. In §3 we report on the saturation of magnetic energy and provide power of spectra various quantities of interest. We also investigate the scaling of various one and two dimensional structure functions of velocity field. In §4 we summarize our findings.

2. METHODS

2.1. RMHD formulation

We have employed Mara, a new unsplit, second-order Godunov code which has been written to achieve robust and accurate evolution of the RMHD equations on three-dimensional rectilinear grids. Mara solves the system of ideal RMHD equations in conservation law form. The covariant formulation for RMHD can be expressed as a system of coupled conservation laws for particle number $N^\mu = \rho u^\mu$ and the energy-momentum of the fluid denoted by $T^{\mu\nu} = \rho h^* u^\mu u^\nu + p^* g^{\mu\nu} - b^\mu b^\nu$, where ρ is the rest-mass density of the fluid and u is its four-velocity and we use units for which the speed of light $c = 1$ as follows,

$$\nabla_\nu N^\nu = 0 \quad (1a)$$

$$\nabla_\nu T^{\mu\nu} = 0 \quad (1b)$$

$$\frac{\partial \mathbf{B}}{\partial t} = \nabla \times (\mathbf{v} \times \mathbf{B}) \quad (1c)$$

Here, $b^\mu = F^\mu_\nu u^\nu$ is the magnetic field four-vector, and $h^* = 1 + e^* + p^*/\rho$ is the total specific enthalpy, where $p^* = p_g + b^2/2$ is the total pressure, p_g is the gas pressure and $e^* = e_{th} + b^2/2\rho$ is the total specific energy density with e_{th} being the thermal part. In this study System 1 is closed by the adiabatic equation of state, $p_g = \rho e_{th}(\Gamma - 1)$ with $\Gamma = 4/3$. Since our equation of state is not isothermal are those used in most previous studies (exceptions include Porter et al. (2002)), thermalization of the kinetic energy into internal energy results in a marginal decline of the sonic Mach number throughout the run. This is discussed in more detail in §3.1.

The fact that ρh^* and p^* and b^μ directly effect all aspects of the energy-momentum dynamics of the fluid through their contributions to $T^{\mu\nu}$ means that RMHD turbulence dynamics will contain mode couplings not present in the non-relativistic case. This is because acoustic and RMHD waves will alter eddy dynamics via their modifications to fluid inertia, as mentioned above. In this study, fluctuations in the thermal energy and pressure due to compressive waves will dominate magnetic fluctuations in $T^{\mu\nu}$ since we consider the case with relativistic thermal pressure, $p/\rho \sim 1$, but subdominant magnetic field. Alfvénic RMHD turbulence for

which magnetic energy density is significant or dominant ($b^2/2 \sim \rho$) is also of interest and will form the basis for a future study.

The ideal RMHD equations can also be expressed in flux conservative form amenable to numerical solution as

$$\frac{\partial \mathbf{U}}{\partial t} + \sum_{j=1}^3 \frac{\partial \mathbf{F}^j}{\partial x^j} = 0 \quad (2)$$

where the conserved quantities

$$\mathbf{U} = \begin{pmatrix} D \\ \tau \\ \mathbf{S} \\ \mathbf{B} \end{pmatrix} = \begin{pmatrix} \rho W \\ \rho h^* W^2 - p^* - (b^0)^2 - D \\ \rho h^* W^2 \mathbf{v} - b^0 \mathbf{b} \\ \mathbf{B} \end{pmatrix} \quad (3)$$

represent the lab frame particle number, total energy (excluding rest mass), momentum, and magnetic induction respectively, and the corresponding fluxes are

$$\mathbf{F}^j = \begin{pmatrix} D v^j \\ \tau v^j - b^0 B^j / W + p^* v^j \\ \mathbf{S} v^j - \mathbf{b} B^j / W + p^* \hat{\mathbf{x}}^j \\ -(\delta_k^m \delta_l^j - \delta_k^j \delta_l^m) v^k B^l \hat{\mathbf{x}}_m \end{pmatrix}. \quad (4)$$

By introducing the volume averaged conserved quantities,

$$\mathbf{U}_{i,j,k} = \frac{1}{\Delta V} \int_{x_{i-1/2}}^{x_{i+1/2}} \int_{y_{j-1/2}}^{y_{j+1/2}} \int_{z_{k-1/2}}^{z_{k+1/2}} \mathbf{U}(\mathbf{x}, t) dV \quad (5)$$

and rewriting Equation 2 using the divergence theorem, we obtain volume averaged time derivatives in each zone,

$$\begin{aligned} \frac{\partial}{\partial t} \mathbf{U}_{i,j,k} = & -\frac{1}{\Delta x} \left(\hat{\mathbf{F}}_{i+1/2,j,k}^1 - \hat{\mathbf{F}}_{i-1/2,j,k}^1 \right) \\ & -\frac{1}{\Delta y} \left(\hat{\mathbf{F}}_{i,j+1/2,k}^2 - \hat{\mathbf{F}}_{i,j-1/2,k}^2 \right) \\ & -\frac{1}{\Delta z} \left(\hat{\mathbf{F}}_{i,j,k+1/2}^3 - \hat{\mathbf{F}}_{i,j,k-1/2}^3 \right) \end{aligned} \quad (6)$$

where $\hat{\mathbf{F}}^j$, are the fluxes of conserved quantities evaluated at the interfaces between cell volumes. Equation 6 would in principle complete the integration scheme for advancing the solution in time. However, in practice an expression which is higher order in time is desirable to maintain accuracy. In this study, Mara has been configured to use a second order unsplit MUSCL-Hancock type integration scheme similar to the one described in Mignone & Bodo (2006), and differs mostly in that magnetic fields are volume instead of area-averaged. The scheme is parameterized around an approximate Riemann solver for obtaining the intercell fluxes $\hat{\mathbf{F}}^j$, and a reconstruction algorithm for interpolating primitive quantities to the zone interfaces. For completeness, the full scheme is described below.

1. Starting with \mathbf{U}^n , invert Equation 3 to obtain \mathbf{P}^n . The primitive quantities are $\mathbf{P} = (\rho, p_g, \mathbf{v}, \mathbf{B})^T$.
2. Compute the spatial derivatives $\frac{\partial \mathbf{P}^n}{\partial x^j}$ in each zone using the reconstruction algorithm, and obtain the

interpolated primitive quantities at the zone interfaces as follows:

$$\begin{aligned}\mathbf{P}_R^{j,n} &= \mathbf{P}^n + \frac{\partial \mathbf{P}^n}{\partial x^j} \frac{\Delta x^j}{2} \\ \mathbf{P}_L^{j,n} &= \mathbf{P}^n - \frac{\partial \mathbf{P}^n}{\partial x^j} \frac{\Delta x^j}{2}\end{aligned}$$

3. Obtain the conserved quantities $\mathbf{U}_L^{j,n+1/2}$ and $\mathbf{U}_R^{j,n+1/2}$ at the half time-step by applying the approximate Riemann solver for the transverse fluxes $\hat{\mathbf{F}}^{2,3}$, and a Hancock operator for the normal fluxes \mathbf{F}^1 . There is one predicted conserved state $\mathbf{U}^{j,n+1/2}$ for each direction. For example, in the x -direction,

$$\begin{aligned}\mathbf{U}_{i,j,k}^{1,n+1/2} &= \mathbf{U}_{i,j,k}^n - \frac{\Delta t}{2\Delta x} \left[\mathbf{F}^1(\mathbf{P}_{R,i,j,k}^{1,n}) - \mathbf{F}^1(\mathbf{P}_{L,i,j,k}^{1,n}) \right] \\ &- \frac{\Delta t}{2\Delta y} \left[\hat{\mathbf{F}}^2(\mathbf{P}_{R,i,j,k}^{2,n}, \mathbf{P}_{L,i,j+1,k}^{2,n}) - \hat{\mathbf{F}}^2(\mathbf{P}_{R,i,j+1,k}^{2,n}, \mathbf{P}_{L,i,j,k}^{2,n}) \right] \\ &- \frac{\Delta t}{2\Delta z} \left[\hat{\mathbf{F}}^3(\mathbf{P}_{R,i,j,k}^{3,n}, \mathbf{P}_{L,i,j,k+1}^{3,n}) - \hat{\mathbf{F}}^3(\mathbf{P}_{R,i,j,k+1}^{3,n}, \mathbf{P}_{L,i,j,k}^{3,n}) \right]\end{aligned}$$

4. Invert Equation 3 to obtain $\mathbf{P}^{j,n+1/2}$ from $\mathbf{U}^{j,n+1/2}$ for each $j = 1, 2, 3$.
5. Obtain the interpolated primitive quantities at the zone interfaces for the half time step. The spatial gradients are not recomputed, but are reused from the beginning of the time step.

$$\begin{aligned}\mathbf{P}_R^{j,n+1/2} &= \mathbf{P}^{n+1/2} + \frac{\partial \mathbf{P}^n}{\partial x^j} \frac{\Delta x^j}{2} \\ \mathbf{P}_L^{j,n+1/2} &= \mathbf{P}^{n+1/2} - \frac{\partial \mathbf{P}^n}{\partial x^j} \frac{\Delta x^j}{2}\end{aligned}$$

6. Complete the time integration by applying the fluxes obtained from the Riemann solver in each direction.

$$\begin{aligned}\mathbf{U}_{i,j,k}^{n+1} &= \mathbf{U}_{i,j,k}^n \\ &- \frac{\Delta t}{\Delta x} \left[\hat{\mathbf{F}}^1(\mathbf{P}_{R,i,j,k}^{1,n+1/2}, \mathbf{P}_{L,i+1,j,k}^{1,n+1/2}) - \hat{\mathbf{F}}^1(\mathbf{P}_{R,i+1,j,k}^{1,n+1/2}, \mathbf{P}_{L,i,j,k}^{1,n+1/2}) \right] \\ &- \frac{\Delta t}{\Delta y} \left[\hat{\mathbf{F}}^2(\mathbf{P}_{R,i,j,k}^{2,n+1/2}, \mathbf{P}_{L,i,j+1,k}^{2,n+1/2}) - \hat{\mathbf{F}}^2(\mathbf{P}_{R,i,j+1,k}^{2,n+1/2}, \mathbf{P}_{L,i,j,k}^{2,n+1/2}) \right] \\ &- \frac{\Delta t}{\Delta z} \left[\hat{\mathbf{F}}^3(\mathbf{P}_{R,i,j,k}^{3,n+1/2}, \mathbf{P}_{L,i,j,k+1}^{3,n+1/2}) - \hat{\mathbf{F}}^3(\mathbf{P}_{R,i,j,k+1}^{3,n+1/2}, \mathbf{P}_{L,i,j,k}^{3,n+1/2}) \right]\end{aligned}$$

2.2. Riemann Solvers

The fluid state in neighboring volumes is formally interpreted as the initial data of a Riemann problem, the solution for which is frequently sought by means of an exact or approximate Riemann solver and yields the intercell fluxes $\hat{\mathbf{F}}^j$. In this study, we have utilized the HLLD approximate Riemann solver (Mignone et al. 2009), which computes Godunov fluxes at zone interfaces by resolving the fast, Alfvén, and contact waves. The inclusion of these waves in the Godunov flux approximation has been shown to be important for capturing the correct concentration of magnetic energy, relative to

the more diffusive HLLC and HLLC approximate solvers (Beckwith & Stone 2011).

Due to the fact that Mara employs ILES, the (effectively numerical) viscous and resistive scales both occur near the grid spacing and thus the magnetic Prandtl number $Pm = Rm/Re \sim 1$. However, deviations in Pm still occur based on the numerically dissipative behavior of the scheme. Based on qualitative observations, the HLLC solver generates roughly the same amount of numerical diffusion to the density and pressure fields as HLLD, but substantially more to the magnetic field. This is interpreted as the HLLD solver achieving a larger numerical Pm . It is also important to note that as the numerical dissipation goes down, the chances of encountering robustness issues (see §2.4) goes up.

2.3. Magnetic field constraint

In this study, Mara uses volume-averaged magnetic fields which are stored at cell centers. The solenoidal constraint $\nabla \cdot \mathbf{B} = 0$ (evaluated at cell corners) is maintained to machine precision using the constrained transport method of Tóth (2000).

2.4. Robustness

Due to the complex nature of the RMHD equations, robustness concerns are of great importance. In particular, RMHD, and GRMHD codes are known to suffer from failures when inverting Equation 3 in order to obtain the primitive variables from the conserved ones. This inversion can fail when the numerical root finder (e.g. secant or Newton-Rapheson) fails to locate the root due to an insufficiently close initial guess. But it can also fail when the root corresponds to a state with negative pressure. Overcoming these numerical limitations has been a major source of effort in evolving the models used in this study.

The Mara code has been designed with an extensively tested and very robust algorithm for the recovery of primitive variables. When the failure is strictly numerical in nature, it will run through a series of reset values and inversion relations. The default inversion relation used in this study is adapted from Noble et al. (2006) and in the case of an adiabatic equation of state, may be solved using a Newton-Rapheson iteration in the single unknown, $Z \equiv \rho h W^2$.

$$\begin{aligned}v^2 &= \frac{S^2 Z^2 + (\mathbf{B} \cdot \mathbf{S})^2 (B^2 + 2Z)}{(B^2 + Z)^2 Z^2} \\ \tau + D &= \frac{B^2}{2} (1 + v^2) - \frac{(\mathbf{B} \cdot \mathbf{S})^2}{2Z^2} + Z - p_g\end{aligned}$$

The starting value of Z given to the root finder is evaluated from the primitive variables at the previous time step. If a suitable solution is not obtained, then the root finder is restarted using $Z = \sqrt{D^2 + S^2}$, which becomes the exact solution in the limiting case of weak magnetic field and small pressure. If a solution is still not obtained, then the procedure is repeated using an inversion relation adapted from Antón et al. (2006).

$$\begin{aligned}S^2 &= (Z + B^2)^2 \frac{W^2 - 1}{W^2} - (2Z + B^2)^2 \frac{(B^i S_i)^2}{Z^2} \\ \tau + D &= B + Z^2 - \frac{B^2}{2W^2} - \frac{(B^i S_i)^2}{Z^2} - p_g\end{aligned}$$

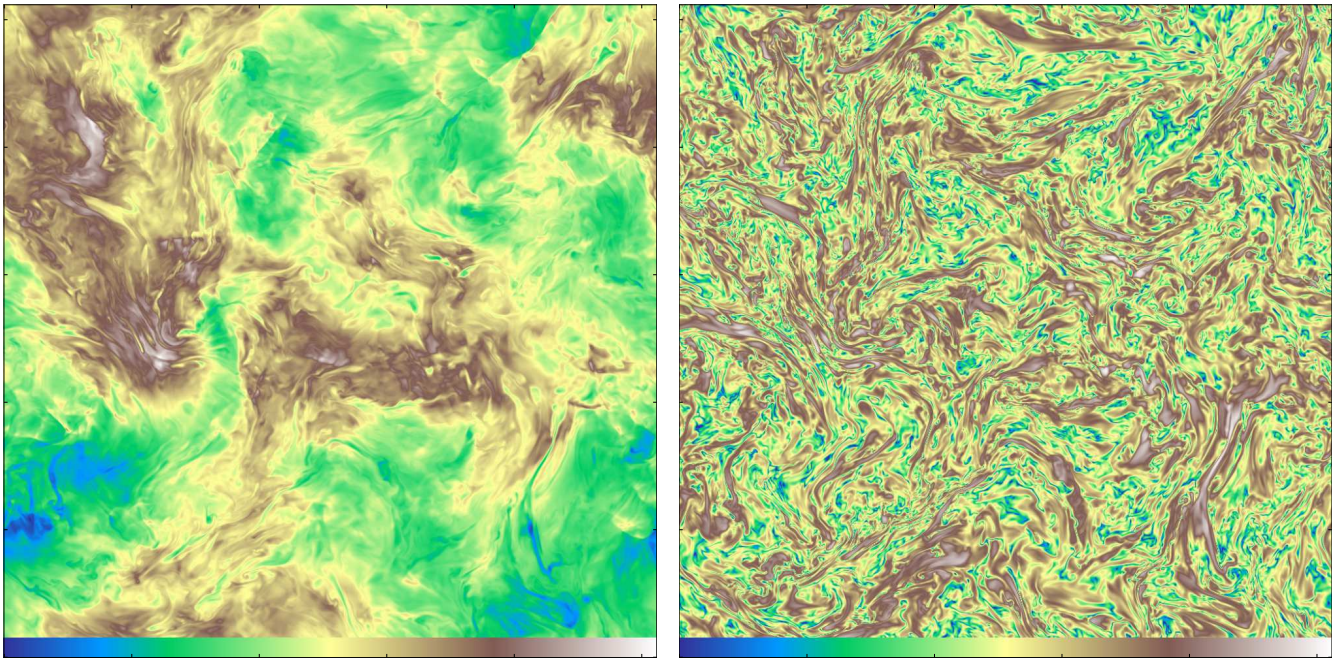


FIG. 1.— Slices of the domain taken at $t = 12.0T_{lc}$, normal to the y -axis. Shown is the rest-mass density (*left*) scaled linearly between 0.326 and 1.53, and the (\log_{10} of) magnetic pressure (*right*), scaled between 3.16×10^{-4} and 1.26.

which can be solved using a two-dimensional Newton-Raphson algorithm for the unknowns Z and W . Because neither of these solvers contains the other one's domain of success, there are circumstances where this procedure obtains the solution even when the first solver or starting value fails. However, there are states whose solution is not obtained by any solver, or whose solution is unacceptable due to negative pressure.

Under these conditions, the code assumes it has integrated the conserved quantities into an unphysical configuration, and requires further safety procedures in order not to crash. The safety feature we have found to be the most practical is the addition of small amounts of diffusion near “unhealthy” zones. This feature is implemented as a Lax-Friedrichs flux, where the failed state $\mathbf{U}_{i,j,k} \mapsto \mathbf{U}'_{i,j,k}$ according to

$$\mathbf{U}'_{i,j,k} = \mathbf{U}_{i,j,k} - \left(\tilde{\mathbf{f}}_{i+1/2,j,k} - \tilde{\mathbf{f}}_{i-1/2,j,k} \right) - \dots \quad (7)$$

where for brevity, we have written the fluxes in the x -direction only, and

$$\tilde{\mathbf{f}}_{i+1/2,j,k} = -\frac{r}{2d} (\mathbf{U}_{i+1,j,k} - \mathbf{U}_{i,j,k}) \theta_{i+1/2,j,k} \quad (8)$$

$d = 3$ is the number of dimensions, and $\theta_{i+1/2,j,k} = 1$ if zones (i, j, k) or $(i + 1, j, k)$ have been flagged as unhealthy, and 0 otherwise. The effect of this prescription is to replace $\mathbf{U}_{i,j,k}$ with a weighted average of itself and the average of its neighboring cells, adding the most diffusion when $r \rightarrow 1$ and none when $r \rightarrow 0$. Throughout this study we have used $r = 0.2$. This formulation for the addition of diffusive terms has several important features. Firstly, it naturally obeys the global conservation of \mathbf{U} , but secondly it obeys the solenoidal magnetic field constraint, because the constrained transport method may be applied to the Lax-Friedrichs magnetic field fluxes be-

fore adding them in Equation 7.

2.5. Initial conditions and driving

Our simulations take place in the periodic cube of length L centered at the origin. We initialize the domain as a uniform and stationary fluid having rest mass density $\rho_0 = 1.0$ and gas pressure $p_g = \rho_0/3$. We apply a uniform magnetic field along the x -direction with magnitude 10^{-3} . The flow is driven stochastically on large scales according to a prescription we have adapted from Schmidt et al. (2009). The driving mechanism is intended to mimic the effect of larger flow structures in which our domain is embedded, and should thus be time-correlated with the turnover time of the largest eddies, which is of order one light-crossing time of the domain, $T_{lc} = L/c$. We achieve smooth time correlation by advancing the Fourier modes $\tilde{\mathbf{a}}(\mathbf{k}, t)$ of the driving field according to an Ornstein-Uhlenbeck process (Uhlenbeck & Ornstein 1930) $d\tilde{\mathbf{a}}(\mathbf{k}, t)$, which consists of a restoring force together with a complex-valued Gaussian-distributed random-walking term, $d\tilde{\mathbf{W}}(\mathbf{k}, t)$:

$$d\tilde{\mathbf{a}}(\mathbf{k}, t) = -\tilde{\mathbf{a}}(\mathbf{k}, t) \frac{dt}{T_{lc}} + \sqrt{\frac{P_{RMS}\sigma^2(\mathbf{k})}{T_{lc}}} \mathfrak{P}(\mathbf{k}) \cdot d\tilde{\mathbf{W}}(\mathbf{k}, t)$$

The projection operator,

$$\mathfrak{P}_{ij}(\mathbf{k}) = \zeta \mathfrak{P}_{ij}^{\perp}(\mathbf{k}) + (1 - \zeta) \mathfrak{P}_{ij}^{\parallel}(\mathbf{k}) \quad (9)$$

is applied to the vector deviate $d\tilde{\mathbf{W}}(\mathbf{k}, t)$ in order to select compressive and vortical driving modes separately, according to the parameter ζ . In this study, we use $\zeta = 1$ which corresponds to a purely vortical driving field. For a detailed study how ζ effects the turbulence statistics, see Federrath et al. (2010).

The acceleration field is applied to the 4-velocity of the flow, u^μ at every time step, $\mathbf{u}(\mathbf{x}, t) \mapsto \mathbf{u}(\mathbf{x}, t) +$

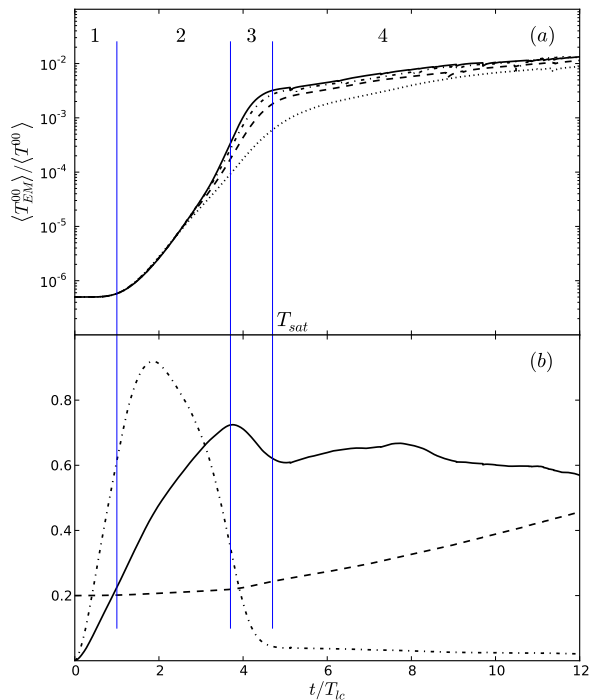


FIG. 2.— (a) Shown are time histories indicating convergence of the magnetic energy fraction, the curves represent different resolutions: dotted: 256^3 , dashed: 512^3 , dash-dotted: 768^3 , solid: 1024^3 . (b) Time histories of various quantities in our highest resolution model, 1024^3 . Shown are the volume-averaged sonic Mach number (solid), Alfvénic Mach number (dash-dotted, divided by 200), and the internal energy (dashed, divided by 5). The Alfvénic Mach number at $t = 12T_{lc}$ is ~ 4 .

$\mathbf{a}(\mathbf{x}, t) dt / u^0$, where the spatial realization is obtained by taking the real part of the Fourier mode superposition

$$\mathbf{a}(\mathbf{x}, t) = \Re \left\{ \sum_{0 < |\mathbf{k}| < K_F} \tilde{\mathbf{a}}(\mathbf{k}, t) \exp(i\mathbf{k} \cdot \mathbf{x}) \right\}. \quad (10)$$

The spectral profile, $\sigma^2(\mathbf{k}) \propto k^6 e^{-8k/k_1}$ (Vestuto et al. 2003; Lemaster & Stone 2009) is normalized to unity over the driven wavenumbers. The length scale of maximum driving, $\ell_1 = 2\pi/k_1$, and the cutoff $\ell_F = 2\pi/K_F$ are chosen to be $L/4$, and $L/2$ respectively. The small subset of driven wavenumbers is chosen for reasons of efficiency, since the evaluation of Equation 10 scales $\propto (2K_F + 1)^3$ and is carried out frequently. The driving mechanism which results from this prescription is time correlated for T_{lc} and has RMS power given by P_{RMS} , which throughout this study has been set to 0.05, delivering a fractional power per light-crossing time, $\langle \dot{E}_{tot} / E_{tot} \rangle T_{lc}$ of between 8% and 10% during the steady-state period of the run. This relatively mild driving power results in a trans-sonic turbulent flow which reaches a quasi-steady state after roughly 5 light-crossing times. We note that no correlation is enforced between real and imaginary parts of $d\mathbf{W}(\mathbf{k}, t)$, and thus the driving field is statistically helicity-free. We refer to the model presented here as SATS1 with the resolution ap-

pendent such that e.g., SATS1-1024 refers to the Super-Alfvénic trans-sonic model 1 at resolution of 1024^3 zones.

3. RESULTS

3.1. Startup transient and quasi-steady evolution

Our model of RMHD turbulence begins with spatially uniform conditions. Therefore, the early evolution of the model is characterized by a startup transient. This transient can be roughly partitioned into three stages, which have been shown in Figure 2. The fourth stage is quasi-steady evolution of the model, and is characterized by very weak magnetic field growth and a thermalization rate balanced by the driving power which causes gradual increase of the internal energy. The results presented in §3 are obtained from six snapshots taken during this phase of the evolution.

About one correlation time of the driving field (T_{lc}) passes before its RMS value is reached. During this stage, gentle driving gradually increases the mean fluid velocity, along with the sonic and Alfvénic Mach numbers. For these Mach numbers, we report the relativistic generalizations (Gedalin 1993)

$$\mathcal{M}_{s,A} = \frac{\beta_f (1 - \beta_f^2)^{-1/2}}{\beta_{s,A} (1 - \beta_{s,A}^2)^{-1/2}} \quad (11)$$

$$\beta_s^2 = \frac{\Gamma p_g}{\rho h} \quad (12)$$

$$\beta_A^2 = \frac{B^2}{B^2 + 4\pi\rho h} \quad (13)$$

where β_f is the fluid velocity.

This stage lasts for only about one T_{lc} , until the driving field is fully “warmed up.” The second stage is characterized by exponential growth of the magnetic energy, and linear growth of kinetic energy. This means that the mean Alfvén velocity increases more rapidly than the bulk velocity, resulting in a sharp drop of the Alfvénic Mach number. The transition to quasi-steady evolution occurs in the third stage and is complete at $4.7T_{lc} = T_{sat}$. During the quasi-steady phase, thermalization at small scales balances the input of kinetic energy at large scales, causing the pressure to gradually increase from 0.333 to 0.720 over the remaining $\sim 7T_{lc}$ duration of this quasi-steady evolution. Also during this stage, magnetic structures gather coherence over larger scales, as demonstrated in Figure 5(c). The fraction of magnetic to total (including thermal) energy increases to 1.5% throughout this phase, and the equipartition scale ($P_K(k) \sim P_B(k)$) reaches $1/5$ the driving scale. Evolution of a 512^3 model (SATS1-512) through $24T_{lc}$ indicates that the magnetic energy fraction stops growing before it reaches 2.0% at which time equipartition occurs at $1/3$ the driving scale. Further discussion of this process is provided in §3.5.

3.2. Universality and locality of compressible turbulence

Universal properties of a turbulent system are those which do not dependent upon any boundary, initial, driving, or dissipative conditions. The goal of many numerical turbulence investigations is to establish universal relations within turbulent fields at different length scales, since by extrapolation they can be used to characterize natural systems whose Reynolds numbers are far greater

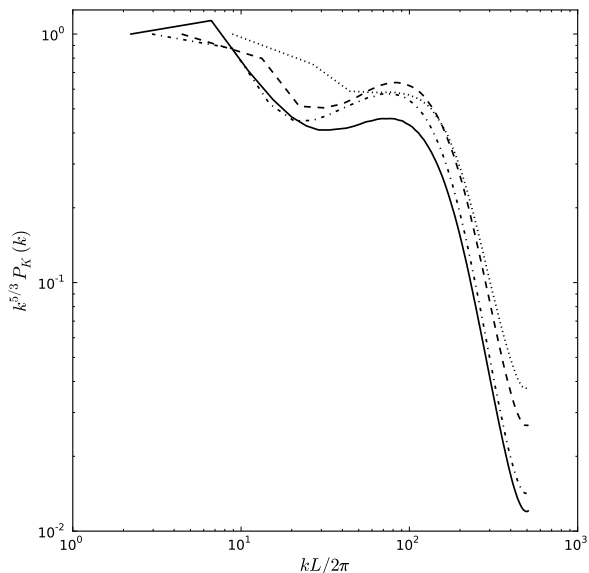


FIG. 3.— Convergence study for the power spectrum of the velocity, $P_K(k)$. Shown are the averaged power spectra, compensated by $k^{5/3}$ for the same model at three different resolutions, 512^3 (dashed), 768^3 (dash-dotted), and 1024^3 (solid).

than those reached by the numerical model. Universal behavior is expected to emerge when the outer and inner scales of turbulence are separated far enough that effects of driving and dissipation are “forgotten” in an intermediate range. Exactly what is meant by “far enough” depends on the degree with which interactions can take place between eddies of disparate sizes. When only eddies of comparable sizes are able to exchange energy, the cascade is said to be highly localized. On the other hand, if energy is capable of flowing directly between structures separated by large wavenumber, the system is said to exhibit nonlocality in its cascade. For such systems, enormously large numerical resolution may be required in order to resolve universal behavior.

The locality hypothesis for incompressible flows (Kolmogorov 1941) led to the well-verified prediction that the power in the velocity field, $P_K(k)$ obeys a power law $\propto k^{-5/3}$ throughout the inertial range. There are now strong arguments that locality holds for compressible turbulence as well (Aluie 2011). In both compressible and incompressible MHD, the dynamics of the cascade are substantially more complicated, and nonlocality or “diffuse locality” (Beresnyak & Lazarian 2009, 2010) is expected to hinder the emergence of universal scalings in presently available numerical experiments. With regard to the likelihood that our simulations are capable of resolving universality, we suggest two reasons to be optimistic. The first is that Porter et al. (2002) have shown that at $\mathcal{M}_S \sim 1$ the turbulent energy transfer is still consistent with the Kolmogorov (1941) theory for incompressible turbulence, meaning that locality is likely to be obeyed. The second is that the nonlocality observed by Beresnyak & Lazarian (2009) is for Alfvénic turbulence in the presence of a strong background magnetic field. For our conditions of fully de-

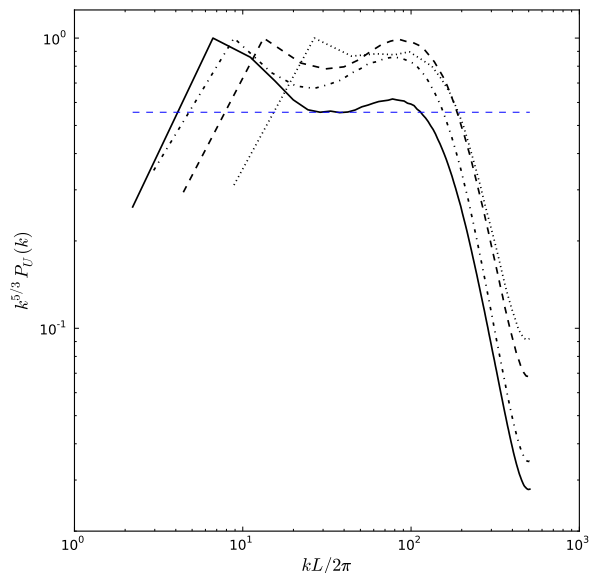


FIG. 4.— Convergence study for the power spectrum of the density-weighted velocity, $P_U(k)$ where $U = \rho^{1/3}v$. Shown are the averaged power spectra, compensated by $k^{5/3}$ for the same model at three different resolutions, 512^3 (dashed), 768^3 (dash-dotted), and 1024^3 (solid).

veloped super-Alfvénic turbulence with no substantial mean field, Verma et al. (2005) predict that the energy transfer is local as long as the net helicity is zero. Since our driving mechanism is helicity-free, this assumption is certainly met. Thus while power law scalings are not guaranteed, they should also not be ruled out *a priori* on the basis of distant wavenumber interactions.

3.3. Convergence study for the power spectrum

Here we assess the degree to which our simulations have resolved the dynamics of the inertial interval by studying the power spectrum of the same model at different grid resolutions. Careful judgement must be used when searching for power law scalings in turbulence power spectra. Generally, one searches the power spectrum for a “flat” interval between two systematic over-densities of power at both ends of the spectrum. At high wave numbers, the so-called “bottleneck” effect (Falkovich 1994) causes a pile-up of power between the inertial and dissipation scales. At low wave numbers, a sort of inverse bottleneck occurs as energy rushes away from the driving scale.

We have computed power spectra of the velocity, $P_K(k)$ and the density-weighted velocity (Kritsuk et al. 2007) $P_U(k)$, where $U \equiv \rho^{1/3}v$ for the same model at the resolutions $N_{res} = 256^3, 512^3, 768^3$, and 1024^3 . It is important to point out that our interpretation of the resolution study is that the size of the grid spacing is kept fixed between runs, so that the box size is reduced to $L \times N_{res}/1024$, and the driving field is moved to higher wavenumber. In this interpretation, the power spectra are compared to one another at the same number of light-crossing times of the largest box size.

Figure 3 shows the power in the velocity field at each

resolution. The main observation is that no inertial range is uncovered for the velocity field, but that the bottleneck (peaking at $kL/2\pi \sim 10^2$) is becoming less pronounced at higher resolution. Figure 4 on the other hand, presents a compelling case that inertial behavior has been resolved for the density weighted velocity $\rho^{1/3}v$ put forward by Kritsuk et al. (2007), and further studied in Kowal & Lazarian (2007); Schmidt et al. (2008); Federrath et al. (2010). We believe that this demonstrates consistency with the prediction of their simple cascade model that $P_U(k) \propto k^{-5/3}$, as well as their numerical findings for highly compressible hydrodynamical turbulence. We note that Lemaster & Stone (2009) have also measured $P_U(k)$ in trans-Alfvénic MHD turbulence at $\mathcal{M}_S \sim 6$ and obtained a much shallower slope of -1.29 . We interpret this as evidence that the cascade model of Kritsuk et al. (2007) may be applicable to super-Alfvénic, but not trans-Alfvénic flows. This interpretation is consistent with observations made by Boldyrev et al. (2002a) that the low-order hydrodynamic statistics of super-Alfvénic turbulence should closely resemble those from the purely hydrodynamical case.

3.4. Power in compressive versus vortical motions

As the Mach number of turbulence increases, so does the degree of fluid compressibility. This means that more of the power in the velocity field is contained in compressive (dilating or shock-like) structures. In order to observe the scale dependence of this effect, we have decomposed the velocity field into solenoidal (curl-like) and dilatational (divergence-like) parts using a Helmholtz decomposition,

$$P_C(\mathbf{k}) = |\hat{\mathbf{k}} \cdot \tilde{\mathbf{v}}_{\mathbf{k}}|^2 \quad (14a)$$

$$P_S(\mathbf{k}) = |\hat{\mathbf{k}} \times \tilde{\mathbf{v}}_{\mathbf{k}}|^2 \quad (14b)$$

The power $P_C(k)$ in compressive modes is shown in Figure 5(a). $P_C(k)$ follows a power law $\propto k^{-1.84}$ over the wavenumbers $k/2\pi \in [7, 31]$, and no bottleneck is observed. The lack of bottleneck in compressive modes has also been observed by (e.g. Porter et al. 1999), while a very similar slope, $k^{-1.79}$, was observed in Federrath et al. (2010). The ratio $P_C(k)/P_K(k)$ of compressive to total power in the velocity field is shown in Figure 5(b). Due to the fact that power is injected at large scales using strictly solenoidal modes, there is an under-density of compressive power at low wavenumber. As the details of energy injection are “forgotten” at smaller scales, the power in compressive modes gradually increases toward moderate wavenumber, reaching a maximum 9% of the total between the inertial and dissipative range. At yet higher wavenumbers through the dissipative range, shearing motions become more significant, but eventually give way to shocklets, causing another rise in the compressive power near the grid scale. The overall trend across scales is that $\sim 5\%$ of the total power is contained in dilatational motion of the fluid, similar to what was found by Porter et al. (2002) for $\mathcal{M}_S \sim 1$ flows. It is interesting to note for non-relativistic highly supersonic ($\mathcal{M}_S \sim 10$) but otherwise very similar conditions, Boldyrev et al. (2002a) found that $P_C(k)/P_K(k) \sim 10\% - 20\%$ through the inertial range, observing a very similar profile to that shown in

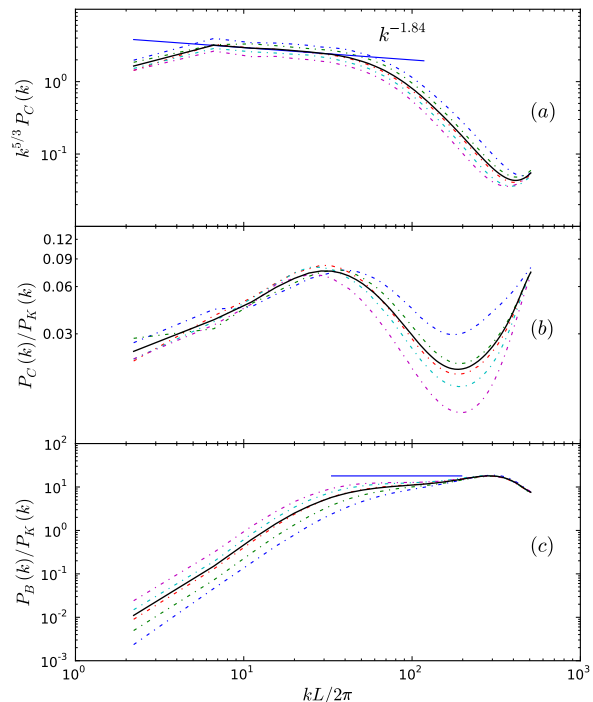


FIG. 5.— Different power spectra taken over the range of times $T_{lc} = 8, 9, 10, 11, 12$ (dash-dotted) and the corresponding time averaged power spectrum (solid). (a): $P_C(k)$, the power in compressive velocity modes at wavenumber k , compensated by $k^{5/3}$. The blue line has a slope -1.84 and is fit over the wave numbers $k/2\pi \in [7, 31]$. Later times are at lower value than earlier times. (b): $P_C(k)/P_K(k)$, the ratio of compressive to total power in the velocity field. Snapshots taken at later times dip lower at moderate to high wavenumber. (c): $P_B(k)/P_K(k)$, the ratio of magnetic to kinetic power at wavenumber k . The trend is that this ratio increases in time at low and moderate wavenumber.

Figure 5(b). Federrath et al. (2010) have studied the effect of driving solenoidal versus dilatational modes in $\mathcal{M}_S \sim 5$ models the ratios $1/3$ and $1/2$ respectively. In their study, these ratios are constant over the inertial range.

As far as convergence to a quasi-stationary state is concerned, we consider the curves in Figure 5(a) to be robust, because only the overall normalization is changing from one snapshot to the next. However, there is a definite time trend in the shape of $P_C(k)/P_K(k)$, indicating that further time evolution would be required to obtain a time-converged measurement of the compressive to total power ratio at different wavenumbers.

3.5. Power spectrum of magnetic energy

Figure 5(c) shows the ratio $P_B(k)/P_K(k)$ of power in the magnetic field to power in the velocity field. The ratio gradually increases from $\sim 1\%$ at the driving scale, through to super-equipartition at the beginning of the dissipative range. It then transitions to become constant across scales throughout the dissipative range. Although the ratio is still changing in time, with more coherence of magnetic structures occurring at large scale, we have

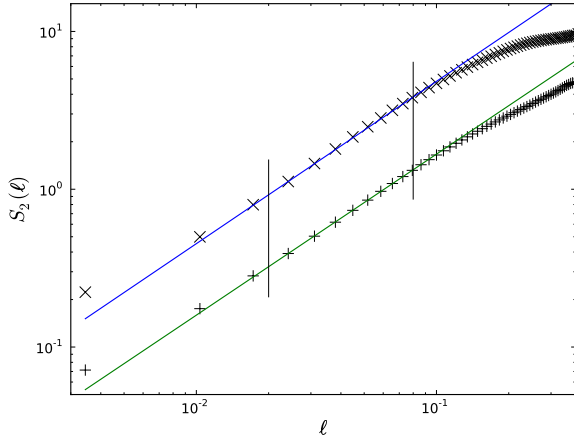


FIG. 6.— Shown is the one-dimensional, second order structure function of the velocity field $S_2^\perp(\ell)$ (\times 's) and $S_2^\parallel(\ell)$ ($+$'s). They are fit by power laws $S_2(\ell) \propto \ell^{\zeta_2}$ with $\zeta_2^\perp = 1.03$ and $\zeta_2^\parallel = 1.02$, where $21\Delta < \ell < 82\Delta$.

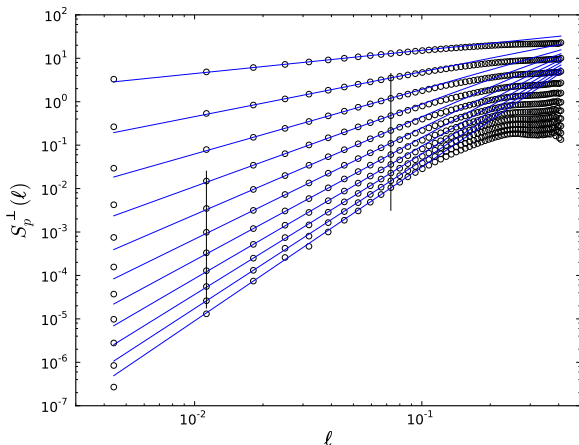


FIG. 7.— One-dimensional, p th order structure function of the velocity field $S_p^\perp(\ell)$, with $p = 1$ (top) to $p = 11$ (bottom).

observed time converged behavior in a 512^3 simulation which was run over a longer time. In doing so, we conclude that the interpretation of Figure 5(c) is robust. After saturation, the ratio of magnetic to kinetic power stays constant over the dissipative range, and obeys a very straight power law throughout the driving and inertial ranges, increasing from low to moderate wavenumber. The scale at which the ratio $P_B(k)/P_K(k) = 1$ occurs at $k \sim 5K_F$ (see §2.5) in the most recent snapshot. However, the trend is for the equipartition scale to move to lower wave number as magnetic structures form coherence over larger scales. Cho & Vishniac (2000b) have observed that once fully steady state is reached, the equipartition scale occurs at $k \sim 3K_F$.

3.6. One dimensional structure functions of the velocity

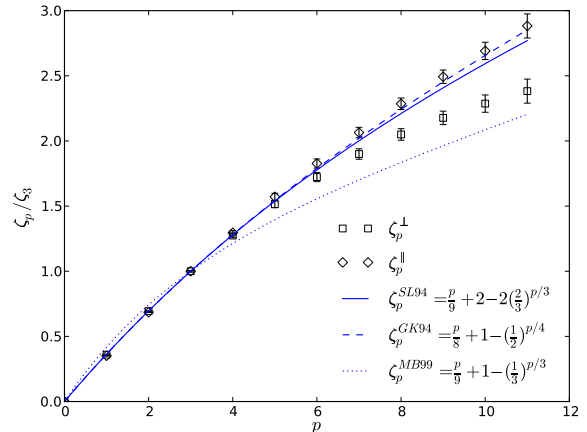


FIG. 8.— The slope ζ_p^\perp (boxes) and ζ_p^\parallel (diamonds) for different values of the order p . The error bars are obtained by shifting the fit window by a single bin. Shown also are the predictions of She & Leveque (1994) (solid) for incompressible non-relativistic hydro turbulence, Grauer et al. (1994) (dashed) and Müller & Biskamp (2000) (dotted) for incompressible MHD turbulence. All data have been normalized by ζ_3 .

We have measured the structure functions of the velocity field to order p ,

$$S_p^{\parallel,\perp}(\ell) = \langle |v^{\parallel,\perp}(\mathbf{r} + \ell) - v^{\parallel,\perp}(\mathbf{r})|^p \rangle$$

where the velocity vector is decomposed in parallel and perpendicular components relative to the displacement vector ℓ . She & Leveque (1994), have determined based on very general assumptions that these functions should scale $\propto \ell^{\zeta_p}$ within the inertial range of fully developed incompressible turbulence, where

$$\zeta_p = \frac{p}{9} + 2 - 2\left(\frac{2}{3}\right)^{p/3} \quad (15)$$

These predictions have been extended analytically to incompressible MHD turbulence (Grauer et al. 1994) and verified numerically (Politano et al. 1995; Müller & Biskamp 2000). The compressible MHD case has been studied numerically by Boldyrev et al. (2002b) and Padoan et al. (2004) in the context of supersonic molecular cloud turbulence, finding remarkably good agreement with analytical predictions.

Figure 6 shows both $S_2^\parallel(\ell)$ and $S_2^\perp(\ell)$. We find that over the range $21\Delta < \ell < 82\Delta$, the structure functions are described by a power law with index $\zeta_2 = 1.025 \pm 0.005$. The high precision of this fit does not rule out systematic errors, but it does imply that some degree of scale-invariant behavior has been resolved in our simulations. The range over which the fit is valid occurs at smaller scales than what was reported by Kritsuk et al. (2007) (32Δ to 256Δ) but very similar to those found by Boldyrev et al. (2002b) (10Δ to 90Δ). The slope $\zeta_2 = 1.025$ is slightly steeper than what was observed by Kritsuk et al. (2007), and considerably steeper than the value of $2/3$ which follows from the Kolmogorov (1941) theory. We also observe that the ratio $S_2^\perp/S_2^\parallel = 2.5$ is larger by a factor of 2 than what was seen in Kritsuk et al. (2007), whose result is in closer

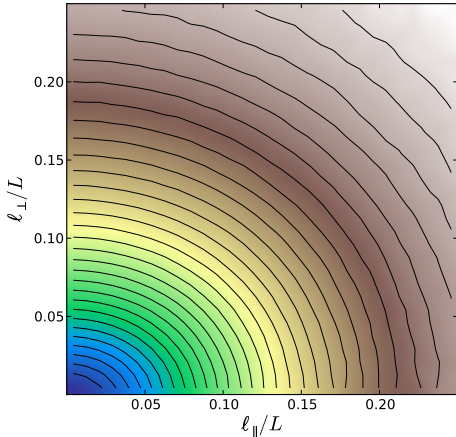


FIG. 9.— Shown is the two-dimensional, second order structure function of the velocity field $S_2^v(\ell_\perp, \ell_\parallel)$. The offset vector ℓ is decomposed into components parallel (x -axis) and perpendicular (y -axis) to the local magnetic field, $\frac{1}{2}(\mathbf{B}(\mathbf{r} + \ell) + \mathbf{B}(\mathbf{r}))$.

agreement with the (Kolmogorov 1941) theory. This observation warrants farther attention, since if the discrepancy is not numerical in nature, but a feature of relativistic MHD turbulence then it may provide important hints in seeking a relativistic extension to the She & Leveque (1994) model.

Using about 10^9 sample pairs, we have been able to compute the slopes of higher order structure functions through $p = 11$. Figure 7 demonstrates the quality of these fits for each order. We have used the same window to compute the slope of the higher order structure functions as for the S_2 case. Figure 8 shows the slopes ζ_p for the transverse and longitudinal structure functions for each p , normalized by ζ_3 . Also shown are the predictions of She & Leveque (1994) for incompressible non-relativistic hydro turbulence, Grauer et al. (1994) and Müller & Biskamp (2000) for incompressible MHD turbulence. We find a remarkable agreement between the Grauer et al. (1994) prediction and the longitudinal velocity fluctuations, even at the highest order. The data for transverse velocity fluctuations lie midway between the Müller & Biskamp (2000) prediction.

3.7. Scale-dependent anisotropy of the velocity field

MHD turbulence in the presence of a strong background field, known as Alfvénic turbulence, consists of an energy cascade mediated by interacting MHD waves. This situation is treatable with the formalism of wave turbulence (see e.g. Zakharov et al. 1992), whereby the resonant interactions between the MHD “free particles” (solutions to the linearized equations) are treated perturbatively. For incompressible MHD, the only free particles are the shear and pseudo Alfvén waves. Analysis of the resonant nonlinear interaction of these modes lead to the model of Goldreich & Sridhar (1995) which predicts a Kolmogorov-like energy spectrum $\propto k^{-5/3}$. Their findings also included the so-called scale-dependent anisotropy with respect to the local mean field, $k_\parallel \propto k_\perp^{2/3}$. This phenomenon is understood geometrically as the exaggerated distortion of eddies, becoming

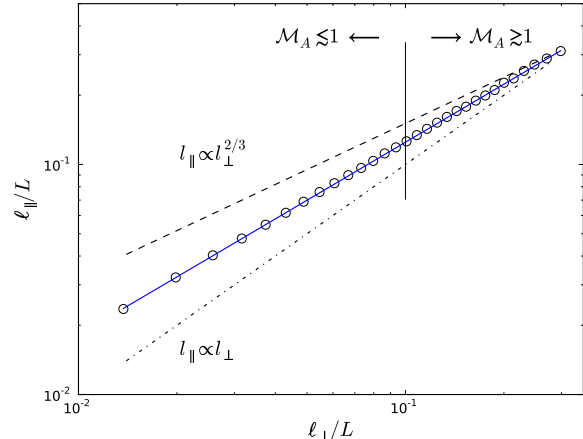


FIG. 10.— The semi-major (ℓ_\parallel) and semi-minor (ℓ_\perp) axes of the elliptical contours obtained from Figure 9 (circles), and the best fit line (solid) $\ell_\parallel \propto \ell_\perp^{0.84}$. For comparison we provide the prediction of Goldreich & Sridhar (1995) $\ell_\parallel \propto \ell_\perp^{2/3}$ (dashed) and a slope of unity (dash-dotted). The vertical line marks the scale $\ell = L/10$ at which the magnetic and kinetic energy are in equipartition.

more apparent at smaller scales. The numerical verification was first obtained by Cho & Vishniac (2000a), who presented two methods of numerical measurement corresponding to the correct geometrical interpretation. Other numerical studies have observed the same scaling in supersonic MHD turbulence (Cho & Lazarian 2003; Beresnyak et al. 2005) and force-free relativistic Alfvénic MHD turbulence (Cho 2005), the latter having received prior analytical treatment by Thompson & Blaes (1998). Here we provide the corresponding measurement for super-Alfvénic, compressible relativistic MHD turbulence.

We use the same method proposed by Cho & Vishniac (2000a) to measure the scale-dependence of eddy distortions, which relies on the eccentricities of level-surfaces for the second order structure functions

$$S_2^v(\ell_\perp, \ell_\parallel) = \langle |\mathbf{v}(\mathbf{r} + \ell) - \mathbf{v}(\mathbf{r})|^2 \rangle \quad (16)$$

$$S_2^B(\ell_\perp, \ell_\parallel) = \langle |\mathbf{B}(\mathbf{r} + \ell) - \mathbf{B}(\mathbf{r})|^2 \rangle \quad (17)$$

where ℓ is decomposed into cylindrical coordinates oriented along the local mean field, which is defined for each pair of points as $\frac{1}{2}(\mathbf{B}(\mathbf{r} + \ell) + \mathbf{B}(\mathbf{r}))$.

In examining the shape of eddies, Cho & Vishniac (2000a) used the structure functions for the velocity and magnetic field S_2^v and S_2^B , finding slopes which were on average slightly larger than $2/3$ for S_2^v and slightly smaller for S_2^B . As depicted in Figure 1(b), coherent magnetic field structures exist out to only about $1/10$ of the domain size, meaning that S_2^B provides a rather narrow window over which to measure the scaling. However, the velocity field is coherent out the driving scale which affords a broad range of scales over which S_2^v scales robustly.

Indeed, we observe excellent scaling in the structure functions of velocity, indicating that the slope $\ell_\parallel \propto \ell_\perp^{0.84}$ is very robust. In fact, the validity of the fit is valid at least between 12Δ and 300Δ , the limiting factor in extending the scaling being due to data collection tech-

niques. The fact that the slope is steeper than the 2/3 means that the eddy distortions depend upon the scale more weakly than in the Goldreich & Sridhar (1995) model. This may suggest corrections to the cascade dynamics to account for relativistic effects, but we forgo any conclusions on this matter until a detailed comparative study with the equivalent non-relativistic case has been completed.

It is also very interesting that the same power law slope of 0.84 holds above and also below the equipartition scale. Under non-relativistic super-Alfvénic conditions, Cho & Vishniac (2000b); Cho & Lazarian (2003) both find similar contour shapes to those shown in Figure 9. However, in those studies the contour intercepts were not provided, meaning that the precise scaling behavior above and below the equipartition scale is uncertain to us. Beresnyak et al. (2005) does provide these scalings for trans-Alfvénic, supersonic conditions, but only below the equipartition scale. We believe that a rigorous study of scaling above and below the equipartition scale in super-Alfvénic turbulence is required in order to isolate the effects of compressibility, substantial magnetic field curvature, and also relativistic effects.

4. CONCLUSIONS

We have measured spectral and scaling properties of relativistically warm magnetohydrodynamic turbulence in the mildly compressible and super-Alfvénic regime. The numerical models were simulated at very high resolution (1024^3) using Mara, a new second order Godunov code tuned for accurate and robust evolution of the RMHD equations in three dimensions. Our main production model was driven stochastically at large scales during quasi-steady evolution for about 6 light-crossing times of the domain. We find that:

1. The magnetic energy is amplified from seed fields to 1.5% of the total fluid energy. The scale at which equipartition between magnetic and kinetic energy occurs is between 1/5 and 1/3 of the driving scale.
2. At 1024^3 the power spectrum of velocity is dominated by a bottleneck, but not inconsistent with the Kolmogorov prediction of $k^{-5/3}$. The power spectrum of density-weighted velocity $\rho^{1/3}v$ scales $\propto k^{-5/3}$ over moderate wavenumbers, consistent with the simple cascade model of Kritsuk et al. (2007).

3. About 5% of kinetic energy is in compressive modes. These modes follow a power law over large to moderate scales with index -1.84 .
4. The transverse and longitudinal one dimensional structure functions of velocity are well fit by a power law over moderate to small scales. As a function of the order p , the slope of longitudinal velocity fluctuation is well described by the prediction of She & Leveque (1994). Statistically significant deviation is observed for the transverse fluctuation.
5. Mild elongation of coherent velocity structures along the local magnetic field is observed. The degree of elongation is scale-dependent, but more weakly than is predicted by Goldreich & Sridhar (1995). The scale dependence obeys a power law to high precision above and below the equipartition scale.

These results suggest that for trans-sonic, super-Alfvénic relativistic astrophysical conditions the turbulent cascade dynamics share many similarities with their non-relativistic counterparts. However, the high order scaling relations developed for non-relativistic media, as well as the Alfvénic cascade model of Goldreich & Sridhar (1995) may require modification in order to be applicable to the relativistic astrophysical environments. A detailed comparison between non-relativistic and relativistic MHD models is currently in progress and will form the basis for a future publication.

This research was supported in part by the NSF through grant AST-1009863 and by NASA through grant NNX10AF62G issued through the Astrophysics Theory Program. Resources supporting this work were provided by the NASA High-End Computing (HEC) Program through the NASA Advanced Supercomputing (NAS) Division at Ames Research Center. We would like to thank the Institute for Theory and Computation at the Harvard-Smithsonian Center for Astrophysics for hospitality, where a portion this work was completed. We thank Andrey Beresnyak for helpful suggestions regarding measurement techniques, and Paul Duffell for many useful discussions. We would also like to acknowledge the developers of the Python `numpy`, `matplotlib`, and `h5py` modules, which were used extensively in our figures and analysis.

REFERENCES

- Aluie, H. 2011, *Phys Rev Lett*, 106, 174502
- Antón, L., Zanotti, O., Miralles, J. A., Martí, J. M., Ibáñez, J. M., Font, J. A., & Pons, J. A. 2006, *The Astrophysical Journal*, 637, 296
- Antonucci, R. 1993, In: *Annual review of astronomy and astrophysics*. Vol. 31 (A94-12726 02-90), 31, 473
- Beckwith, K., & Stone, J. M. 2011, *The Astrophysical Journal Supplement*, 193, 6
- Begelman, M. C., Blandford, R. D., & Rees, M. J. 1984, *Reviews of Modern Physics*, 56, 255
- Beresnyak, A., & Lazarian, A. 2009, *The Astrophysical Journal*, 702, 1190
- . 2010, *The Astrophysical Journal Letters*, 722, L110
- Beresnyak, A., Lazarian, A., & Cho, J. 2005, *The Astrophysical Journal*, 624, L93
- Boldyrev, S., Nordlund, Å., & Padoan, P. 2002a, *The Astrophysical Journal*, 573, 678
- . 2002b, *Phys Rev Lett*, 89, 31102
- Burkhart, B., Falceta-Gonçalves, D., Kowal, G., & Lazarian, A. 2009, *The Astrophysical Journal*, 693, 250
- Cho, J. 2005, *The Astrophysical Journal*, 621, 324
- Cho, J., & Lazarian, A. 2003, *Monthly Notices of the Royal Astronomical Society*, 345, 325
- Cho, J., & Vishniac, E. T. 2000a, *The Astrophysical Journal*, 539, 273
- . 2000b, *The Astrophysical Journal*, 538, 217
- Falkovich, G. 1994, *Physics of Fluids*, 6, 1411
- Federrath, C., Roman-Duval, J., Klessen, R. S., Schmidt, W., & Low, M.-M. M. 2010, *Astronomy and Astrophysics*, 512, 81
- Fox, D. B., & Mészáros, P. 2006, *New Journal of Physics*, 8, 199

- Frank, J., King, A., & Raine, D. J. 2002, *Accretion Power in Astrophysics*, ISBN: 0521620538
- Gedalin, M. 1993, *Physical Review E (Statistical Physics)*, 47, 4354
- Gehrels, N., Ramirez-Ruiz, E., & Fox, D. B. 2009, *Annual Review of Astronomy & Astrophysics*, 47, 567
- Goldreich, P., & Sridhar, S. 1995, *Astrophysical Journal*, 438, 763
- Grauer, R., Krug, J., & Marliani, C. 1994, *Physics Letters A*, 195, 335
- Kolmogorov, A. N. 1941, *Proceedings: Mathematical and Physical Sciences*, 434, 9
- Kowal, G., & Lazarian, A. 2007, *The Astrophysical Journal*, 666, L69
- . 2010, *Astrophysical Journal*, 720, 742
- Kritsuk, A. G., Norman, M. L., Padoan, P., & Wagner, R. 2007, *The Astrophysical Journal*, 665, 416
- Kritsuk, A. G., Ustyugov, S. D., Norman, M. L., & Padoan, P. 2009, *Journal of Physics: Conference Series*, 180, 2020
- Krolik, J. H. 1999, *Active galactic nuclei : from the central black hole to the galactic environment* / Julian H. Krolik. Princeton
- Lemaster, M. N., & Stone, J. M. 2009, *The Astrophysical Journal*, 691, 1092
- Maron, J., & Goldreich, P. 2001, *The Astrophysical Journal*, 554, 1175
- Mignone, A., & Bodo, G. 2006, *Monthly Notices of the Royal Astronomical Society*, 368, 1040
- Mignone, A., Ugliano, M., & Bodo, G. 2009, *Monthly Notices of the Royal Astronomical Society*, 393, 1141
- Müller, W.-C., & Biskamp, D. 2000, *Phys Rev Lett*, 84, 475
- Noble, S. C., Gammie, C. F., McKinney, J. C., & Zanna, L. D. 2006, *The Astrophysical Journal*, 641, 626
- Padoan, P., Jimenez, R., Nordlund, Å., & Boldyrev, S. 2004, *Phys Rev Lett*, 92, 191102
- Padoan, P., Jones, B. J. T., & Nordlund, A. P. 1997, *Astrophysical Journal* v.474, 474, 730
- Piran, T. 2004, *Reviews of Modern Physics*, 76, 1143
- Politano, H., Pouquet, A., & Sulem, P. L. 1995, *Physics of Plasmas*, 2, 2931
- Porter, D., Pouquet, A., Sytine, I., & Woodward, P. 1999, *Physica A*, 263, 263
- Porter, D., Pouquet, A., & Woodward, P. 2002, *Physical Review E*, 66, 26301
- Schmidt, W., Federrath, C., Hupp, M., Kern, S., & Niemeyer, J. C. 2009, *Astronomy and Astrophysics*, 494, 127
- Schmidt, W., Federrath, C., & Klessen, R. 2008, *Phys Rev Lett*, 101, 194505
- She, Z.-S., & Leveque, E. 1994, *Phys Rev Lett*, 72, 336
- Soderberg, A. M., Chakraborti, S., Pignata, G., Chevalier, R. A., Chandra, P., Ray, A., Wieringa, M. H., Copete, A., Chaplin, V., Connaughton, V., Barthelmy, S. D., Bietenholz, M. F., Chugai, N., Stritzinger, M. D., Hamuy, M., Fransson, C., Fox, O., Levesque, E. M., Grindlay, J. E., Challis, P., Foley, R. J., Kirshner, R. P., Milne, P. A., & Torres, M. A. P. 2010, *Nature*, 463, 513
- Thompson, C., & Blaes, O. 1998, *Physical Review D (Particles)*, 57, 3219
- Tóth, G. 2000, *Journal of Computational Physics*, 161, 605, (c) 2000: Academic Press
- Uhlenbeck, G. E., & Ornstein, L. S. 1930, *Phys. Rev.*, 36, 823
- Vazquez-Semadeni, E., Ostriker, E. C., Passot, T., Gammie, C. F., & Stone, J. M. 2000, *Protostars and Planets IV* (Book - Tucson: University of Arizona Press; eds Mannings, 3
- Verma, M. K., Ayyer, A., & Chandra, A. V. 2005, *Physics of Plasmas*, 12, 2307
- Vestuto, J. G., Ostriker, E. C., & Stone, J. M. 2003, *The Astrophysical Journal*, 590, 858
- Woosley, S. E., & Bloom, J. S. 2006, *Annual Review of Astronomy & Astrophysics*, 44, 507
- Zakharov, V. E., Lvov, V. S., & Falkovich, G. 1992, 264
- Zhang, B., & Mészáros, P. 2004, *International Journal of Modern Physics A*, 19, 2385
- Zhang, W., MacFadyen, A., & Wang, P. 2009, *The Astrophysical Journal Letters*, 692, L40